JOURNAL OF COMPUTATIONAL PHYSICS 87, 396–407 (1990)

Improved Radial Differencing for Three-Dimensional Magnetohydrodynamic Equilibrium Calculations*

S. P. HIRSHMAN

Oak Ridge National Laboratory, Oak Ridge, Tennessee 37831

AND

U. SCHWENN AND J. NÜHRENBERG

Max-Planck Institut für Plasmaphysik, Association IPP-EURATOM, D-8046 Garching bei München, Federal Republic of Germany

Received December 9, 1988; revised April 14, 1989

Several numerical schemes are described for accurately discretizing the radial dependence of the magnetohydrodynamic (MHD) energy of a toroidal plasma configuration. Compared with previous schemes, the new methods have significantly improved mesh convergence properties for the energy, magnetic axis, and other equilibrium parameters. This has favorable implications for both stability analysis, where small numerical errors in the energy may significantly affect the computation of marginal points, and transport applications, for which equilibrium computations on coarse meshes are desirable. © 1990 Academic Press, Inc.

1. INTRODUCTION

A variety of codes that use spectral methods for computing three-dimensional MHD equilibria have been developed [1–4]. The spectral convergence of the finite Fourier representations for the cylindrical coordinates R and Z has been improved [1, 2] through the introduction of a renormalization stream function, λ. The convergence with the radial mesh spacing, Δs, of such characteristic equilibrium quantities as the energy (W) and the axis shift (Δ) also tends to improve in conjunction with accelerated spectral convergence. In general, however, the dependence on Δs of W, Δ, and other equilibrium parameters remains strong enough to necessitate very refined radial grids, in conjunction with mesh extrapolations, to predict the actual ($\Delta s \to 0$) equilibrium configuration [1, 2].

* Research sponsored in part by the Office of Fusion Energy, U.S. Department of Energy, under contract DE-AC05-84OR21400 with Martin Marietta Energy Systems, Inc. The U.S. Government's right to retain a nonexclusive royalty-free license in and to the copyright covering this paper, for governmental purposes, is acknowledged.

0021-9991/90 $3.00

When the spectral components of the equilibrium equations are truncated at a very small number of modes, they can be solved "exactly" (i.e., for $\Delta s \simeq 0$) by using an adaptive spatial integration technique [3]. As the number of spectral modes required to describe most realistic configurations increases ($m \geqslant 2$, $n \geqslant 2$, where m and n are poloidal and toroidal mode numbers, respectively), the convergence of this technique deteriorates, and methods that employ finite radial grids become necessary. The present investigation is concerned with improving the radial mesh convergence properties of these grid techniques by applying accurate finite-differencing algorithms to the radially discretized MHD energy.

The concept of improved mesh convergence may be illustrated by considering the radial mesh dependence of the magnetic energy, W. For a differencing scheme that uses second-order central sums and differences to evaluate quantities and their s derivatives, respectively, at the half-mesh points in radius, it follows that

$$W(\Delta s) = W_\infty \left[1 + \sum_{l=1} \alpha_l (\Delta s)^{2l} \right]. \tag{1}$$

Here, the values of α_l depend only on the finite-difference representation and the spectral mode truncation used to compute W, but they are independent of Δs. The radial mesh convergence is improved whenever the value of $|\alpha_1|$ in Eq. (1) is decreased without increasing the order of the finite-difference approximation for W. (The restriction to second-order differencing is imposed to maintain a reasonable temporal convergence rate for the iterative technique used to solve the finite-differenced moment equations. This also avoids possible numerical errors around rational surfaces where the magnetic field may be discontinuous but integrable.) A smaller $|\alpha_1|$ corresponds to values of W computed on a finite mesh, which are nearer to W_∞ and thus give a better approximation to the actual equilibrium.

The values of $|\alpha_l|$ in Eq. (1) may be affected by the choice of the radial coordinate, s, in relation to the spatial distribution of the toroidal magnetic flux, $\Phi(s)$. Only the two choices $\Phi_1 \propto s$ and $\Phi_2 \propto s^2$ are compared here. The coordinate s is scaled to vary between $s = 0$ at the magnetic axis and $s = 1$ at the plasma boundary. Near the critical point $s = 0$ of the polar "flux" coordinate system, the incremental volume element $V' \equiv dV/ds$ scales with s as $V_1' = \text{constant}$ for Φ_1 and $V_2' \propto s$ for Φ_2, so that locally Φ_1 zoning is an equal volume distribution of points and Φ_2 zoning is similar to a polar distribution. In particular, Φ_1 zoning tends to yield more accurate values for volume-integrated quantities such as W, whereas the polar zoning yields better resolution near the magnetic axis, $s = 0$. Thus, there is a balance between the improvement in the computed values of W that may be afforded by the Φ_1 zoning and the accurate representation of the magnetic axis and other near-axis quantities given by the Φ_2 zoning. This implies that the mesh convergence properties of other equilibrium quantities besides W should also be considered in formulating a criterion for convergence improvement.

The type of radial zoning that yields both good spatial resolution and rapid temporal convergence of the MHD equilibrium equations depends somewhat on

the particular differencing scheme used to represent W. While a detailed analysis of this correlation is difficult, there is numerical evidence which suggests that the correct spatial discretization of the MHD force near the magnetic axis is critical for suppressing numerically unstable eigenvalues associated with the logarithmic singularity of the polar Laplacian near $s=0$. One successful means for treating this critical point is presented in Section 3. It should be noted that unstable spatial eigenvalues manifest themselves as a lack of "temporal" convergence in the second-order Richardson iteration scheme used here [1] to "evolve" the MHD forces to an equilibrium state.

2. Finite-Difference Representations for W

The magnetic portion of the MHD energy is

$$W=\int \frac{B^2}{2\mu_0}\, d^3x, \tag{2}$$

where $B^2=B^\theta B_\theta+B^\zeta B_\zeta=B_R^2+B_Z^2+B_\phi^2$, $B^\theta=l_\zeta/\sqrt{g}$, $B^\zeta=l_\theta/\sqrt{g}$, $B_\theta=B^\theta g_{\theta\theta}+B^\zeta g_{\theta\zeta}$, $B_\zeta=B^\theta g_{\theta\zeta}+B^\zeta g_{\zeta\zeta}$, $l_\zeta=\chi'-\lambda_\zeta$, $l_\theta=\Phi'+\lambda_\theta$, and $d^3x=\sqrt{g}\, d\theta\, d\zeta\, ds$. Here, λ is the periodic stream function appearing in the contravariant representation of the magnetic field, $\mathbf{B}=\Phi'\nabla s\times\nabla\theta-\chi'\nabla s\times\nabla\zeta+\nabla s\times\nabla\lambda$, where $2\pi\Phi(s)$ is the toroidal flux, $2\pi\chi(s)$ is the poloidal flux, and prime denotes d/ds. We adopt the subscript notation $X_\alpha\equiv\partial X/\partial\alpha$, for $X=(R, Z, \lambda)$ and $\alpha=(s, \theta, \zeta)$, to denote differentiation of the cylindrical coordinates and stream function with respect to the local flux coordinate system variables. Here, θ is a poloidal angle and $\zeta=\phi$ is the cylindrical toroidal angle. The cylindrical components of the magnetic field $\mathbf{B}$ are $B_X=B^\theta X_\theta+B^\zeta X_\zeta$ for $X=(R, Z)$ and $B_\phi=RB^\zeta$. (The subscripts on components of $\mathbf{B}$ denote covariant components and should not be confused with the differentiation operation on the coordinates X.) Variations of Eq. (2) with respect to R, Z, and λ yield components of the MHD equilibrium equation, $(\nabla\times\mathbf{B})\times\mathbf{B}-\nabla p=0$. (An additional constraint energy, discussed in [1], must be minimized along with W to uniquely specify the poloidal angle θ which will yield optimally convergent Fourier spectra for R and Z. Other prescriptions for θ are possible [2–4].)

The first differencing scheme considered here will be denoted (I) and was discussed in [1]. In scheme (I), Eq. (2) was evaluated with R, Z, $\Lambda=\lambda/\Phi'$, and $\iota=\chi'/\Phi'$ on the set of integer radial nodes $s_j=(j-1)\,\Delta s$, where $\Delta s=1/(N_s-1)$, $j=1, ..., N_s$, and $R(s_j)\equiv R^j$, etc. The toroidal flux gradient Φ' and the Jacobian $\sqrt{g}$ were both evaluated on the half-integer grid, $s_{j+1/2}\equiv(s_j+s_{j+1})/2$, and the zoning $\Phi'\propto s$ was used. Conservative differencing of the Jacobian was used,

$$\sqrt{g}^{\,j+1/2}=r_\theta^{j+1/2}Z_s^{j+1/2}-r_s^{j+1/2}Z_\theta^{j+1/2}, \tag{3}$$

where $r=\frac{1}{2}R^2$, $X_\theta^{j+1/2}=(X_\theta^j+X_\theta^{j+1})/2$, and $X_s^{j+1/2}=(X^{j+1}-X^j)/\Delta s$, for

$X=(r, Z)$. If these differencing rules are used, the discrete version of Eq. (2) then becomes

$$W=\int d\theta \int d\zeta\, \Delta s \sum_j \left(\frac{\sqrt{g}B^2}{2\mu_0}\right)^{j+1/2}, \tag{4a}$$

where

$$(\sqrt{g}B_\phi^2)^{j+1/2}=\left[\frac{(\Phi')^2}{\sqrt{g}}\right]^{j+1/2}\left\{\frac{[R^2(1+\Lambda_\theta)^2]^j+[R^2(1+\Lambda_\theta)^2]^{j+1}}{2}\right\}, \tag{4b}$$

$$(\sqrt{g}B_X^2)^{j+1/2}=\left[\frac{(\Phi')^2}{\sqrt{g}}\right]^{j+1/2}\left[\frac{(\hat{b}_X^j)^2+(\hat{b}_X^{j+1})^2}{2}\right], \tag{4c}$$

$$\hat{b}_X^j=[(\iota-\Lambda_\zeta)X_\theta+(1+\Lambda_\theta)X_\zeta]^j, \tag{4d}$$

and $X=(R, Z)$.

The discrete MHD forces should in principle result from taking derivatives of Eq. (4a) with respect to the nodal values of R, Z, and Λ. For example, the discrete Λ forces obtained in this way are

$$(\sqrt{g}F_\Lambda)^j=\frac{\partial}{\partial\theta}(\Phi' B_\zeta)^j-\frac{\partial}{\partial\zeta}(\Phi' B_\theta)^j, \tag{5a}$$

where

$$(\Phi' B_\zeta)^j=\left\langle\frac{(\Phi')^2}{\sqrt{g}}\right\rangle^j(R^2+R_\zeta\hat{b}_R+Z_\zeta\hat{b}_Z)^j, \tag{5b}$$

$$(\Phi' B_\theta)^j=\left\langle\frac{(\Phi')^2}{\sqrt{g}}\right\rangle^j(R_\theta\hat{b}_R+Z_\theta\hat{b}_Z)^j. \tag{5c}$$

Here, the brackets $\langle\ \rangle$ represent the following averaging operator over adjacent radial mesh points:

$$\langle A\rangle^j\equiv\begin{cases}\frac{1}{2}(A^{j+1/2}+A^{j-1/2}), & j\neq 1, N_s\\ A^{N_s-1/2}, & j=N_s.\end{cases} \tag{5d}$$

Two features of Eqs. (5) lead to poor spatial convergence properties for W when scheme (I) differencing is used. One is the appearance of $J\equiv\langle(\Phi')^2/\sqrt{g}\rangle^j$ rather than the more accurate averaged quantity $K\equiv\langle\Phi'/\sqrt{g}\rangle^j\langle\Phi'\rangle^j$, and the other is the low-order approximation (in Δs) for $(\Phi')^2/\sqrt{g}$ at the plasma boundary, namely $[(\Phi')^2/\sqrt{g}]^{N_s}\simeq[(\Phi')^2/\sqrt{g}]^{N_s-1/2}$. The implementation of scheme (I) used in [1] replaced J by K (providing better resolution near the magnetic axis) and extrapolated the last two half-grid values of $(\Phi')^2/\sqrt{g}$ to increase, to second order in Δs, the accuracy of the boundary value for this quantity. Both of these local

changes to the discrete forces imply that the discretized W given in Eq. (4a) is strictly minimized only as $\Delta s \to 0$.

The inaccuracies intrinsic to scheme (I) are resolved by representing λ on the half-mesh grid [2, 5]. Now the force $F_\lambda^{j+1/2}$ is proportional to $(\Phi')^2/\sqrt{g}$ evaluated at $s_{j+1/2}$. Therefore, no extrapolation for F_λ is required at the plasma boundary, and accurate discrete representations for the forces can be obtained directly from first principles by differentiating the discretized energy, W. This improved radial differencing scheme for λ has also been incorporated into a recent spectral code [6].

To ensure temporal stability, Eq. (4) must be recast to represent the toroidal magnetic field term B_ϕ arising from R^2 on the half-mesh. Without this form of differencing, a numerical interchange instability results near the magnetic axis. This scheme, denoted here as (IIA), was first used successfully in [2]. There, the identity $R^2/\sqrt{g} = \sqrt{g}/\tau^2$, where $\tau = R_\theta Z_s - R_s Z_\theta$ is the two-dimensional area element, was used to evaluate $\sqrt{g} B_\phi^2$ on the half-grid as follows:

$$(\sqrt{g} B_\phi^2)^{j+1/2} = \left(l_\theta^2 \frac{\sqrt{g}}{\tau^2} \right)^{j+1/2}. \tag{6a}$$

In Eq. (6a), both $\sqrt{g}$ and τ are differenced conservatively, as given by the rule in Eq. (3). Note that all quantities on the right of Eq. (6a) are evaluated naturally (i.e., without recourse to the averaging brackets operator defined in Eq. (5d)) at radial half-mesh points. (The quantities l_θ and l_ζ are defined following Eq. (2).) This feature allows the present discretization to accurately resolve radial derivatives of the components of **B**. Hence, an accurate representation of localized parallel currents can be expected [6, 8] with decreasing mesh size.

The remaining terms that make up $\sqrt{g} B^2$ are discretized as follows:

$$(\sqrt{g} B_X^2)^{j+1/2} = \left(\frac{1}{\sqrt{g}} \right)^{j+1/2} [(l_\zeta^2) X_\theta^2 + 2(l_\zeta l_\theta) X_\theta X_\zeta + (l_\theta^2) X_\zeta^2]^{j+1/2}, \tag{6b}$$

$$(XY)^{j+1/2} = \tfrac{1}{2}[(XY)^j + (XY)^{j+1}]. \tag{6c}$$

Recall that X denotes either R or Z.

A slight variation of this scheme, denoted (IIB), can eliminate the τ^2 denominator in Eq. (6a). The quantity $\sqrt{g} B^2$ is recast as the equivalent expression,

$$\sqrt{g} B^2 = \frac{l_\theta^2 + b_u^2}{\tau_u} + \frac{b_Z^2}{\sqrt{g}}, \tag{7}$$

where $\tau_u = u_\theta Z_s - u_s Z_\theta$, $b_u = l_\zeta u_\theta + l_\theta u_\zeta$, $b_Z = l_\zeta Z_\theta + l_\theta Z_\zeta$, and $u = \ln |R|$. Note the symmetric role of u (which is related to the cylindrical Green's function) and Z in this representation. In contrast to scheme (IIA), $\sqrt{g}/\tau^2$ is now replaced by τ_u^{-1}, and the helical terms (b_u^2) arising from R_ζ are combined naturally with the toroidal field term (l_θ^2). The finite-difference version of Eq. (7) is similar to Eq. (6) with $\tau_u^{j+1/2}$

differenced conservatively and with the discrete forces containing terms of order τ_u^{-2}, in contrast to τ^{-3} terms for the scheme (IIA) forces. This yields slightly improved spatial and temporal convergence properties when scheme (IIB) is used for systems with weak helical axes.

Schemes (IIA) and (IIB) show markedly improved radial convergence properties as compared with scheme (I) when applied to configurations with nearly planar magnetic axes. However, they often exhibit poor temporal convergence and spatial resolution for systems with strong helical axes in which the $(X_\zeta)^2$ terms in Eq. (6b) are significant. When scheme (II) differencing is used for such systems, the ι profile computed from the zero-current condition [7], $\langle \mathbf{J} \cdot \nabla \zeta \rangle = 0$, is found to deviate from its correct linear dependence on Φ near $s = 0$. This results from a numerical discretization error and thus persists even as $\Delta s \to 0$. Specifically, it is the result of inaccurate differencing of $\sqrt{g}$ and $g_{\theta\zeta}$ near the magnetic axis when scheme (II) is used. To correct this, the dominant analytic behavior of R and Z near $s = 0$ must be correctly represented. Let X denote either R or Z. Then, X is decomposed as

$$X = X_e + \sqrt{\Phi} X_o, \tag{8a}$$

where

$$X_e = \sum_{\text{even } m;\, n} X_{mn}(\Phi) \exp[i(m\theta - n\zeta)], \tag{8b}$$

$$X_o = \Phi^{-1/2} \sum_{\text{odd } m;\, n} X_{mn}(\Phi) \exp[i(m\theta - n\zeta)]. \tag{8c}$$

This separation into even and odd poloidal harmonics makes explicit use of the nonanalytic dependence of X on the toroidal flux Φ near the magnetic axis $s = 0$. Because X_e and X_o are individually analytic near $s = 0$, they both have power series expansions [9, 10] in Φ. Thus, when flux zoning $s \propto \Phi$ is used (at least locally near $s = 0$), these two analytic functions may be differenced and summed on the radial s mesh to obtain accurate half-mesh approximations for both radial derivatives and function values, even though the composite quantity X does not share this property. The area element $\tau = R_\theta Z_s - R_s Z_\theta$ now assumes the finite-difference form $\tau^{j+1/2} = \tau_0^{j+1/2} + \tau_1^{j+1/2}$, where

$$\tau_0^{j+1/2} = \tfrac{1}{2}(R_{o\theta} Z_o - R_o Z_{o\theta})^{j+1/2}, \tag{9a}$$

$$\tau_1^{j+1/2} = R_\theta^{j+1/2} \hat{Z}_s^{j+1/2} - \hat{R}_s^{j+1/2} Z_\theta^{j+1/2} + \frac{1}{2\sqrt{s_{j+1/2}}} (R_{e\theta} Z_o - R_o Z_{e\theta})^{j+1/2}. \tag{9b}$$

Here, $\tau_1 \sim O(\sqrt{s})\tau_0$, and therefore τ_0 gives the dominant contribution to the Jacobian near the magnetic axis. Note that, with the choice of flux zoning, $s \propto \Phi$, the modes with $m \leqslant 3$ that make up X_e and X_o are linear functions of s near $s = 0$. Therefore, the contribution to Eq. (9) from these modes is represented accurately by this finite-difference scheme. (This should be compared with the $\sqrt{\Phi}$ zoning

used in scheme (I), where only the $m=0, 1$ mode contributions to τ are correctly represented.) The half-mesh sum rule for products, given in Eq. (6c), applies in Eq. (9). Also, $X_\theta^{j+1/2} \equiv X_{e\theta}^{j+1/2} + \sqrt{s}_{j+1/2} X_{o\theta}^{j+1/2}$ and $\hat{X}_s^{j+1/2} \equiv X_{es}^{j+1/2} + \sqrt{s}_{j+1/2} X_{os}^{j+1/2}$ for $X=(R, Z)$. The explicit extraction and accurate differencing of the dominant τ_0 term in Eq. (9) seem to be responsible for the stability of the present scheme (III) in response to numerical interchanges when half-mesh differencing for λ is used. The differencing of the metric tensor elements $\hat{g}_{\alpha\beta} \equiv R_\alpha R_\beta + Z_\alpha Z_\beta$ is straightforward:

$$\hat{g}_{\alpha\beta}^{j+1/2} = (R_{e\alpha} R_{e\beta} + Z_{e\alpha} Z_{e\beta})^{j+1/2} + \sqrt{s}_{j+1/2} (R_{e\alpha} R_{o\beta} + R_{o\alpha} R_{e\beta} + Z_{e\alpha} Z_{o\beta} + Z_{o\alpha} Z_{e\beta})^{j+1/2} + s_{j+1/2} (R_{o\alpha} R_{o\beta} + Z_{o\alpha} Z_{o\beta})^{j+1/2}. \quad (10)$$

Here, $X_\alpha \equiv \partial X/\partial\alpha$ for $\alpha=(\theta, \zeta)$. Note that the metric element $g_{\theta\zeta}$ is dominated for small values of s by the term varying as $\sqrt{s}_{j+1/2}$ in Eq. (10). The inability of scheme (II) differencing to accurately represent this nonanalytic behavior of $g_{\theta\zeta}$ is responsible for the poor resolution of the ι profile mentioned before.

The scheme (III) differencing just described represents a compromise between an extremely accurate treatment of the radial dependence of X and an almost complete neglect of the analytic behavior of X near the axis. The former case would require the extraction of a factor $\Phi^{m/2}$ for each poloidal mode. This procedure is tedious to implement numerically [10] and results in a degradation in computational speed and stability. The latter case is typified by schemes (I) and (II).

3. Treatment of the Magnetic Axis Critical Point

The numerical treatment of the magnetic axis (coordinate critical point) at $s=0$ depends on the radial behavior (zoning) of $\Phi(s)$ near the axis. The $m=0$ components of R and Z (denoted X) have the following asymptotic behavior as $s \to 0$:

$$X(s) = X(0) + \Phi X'(0) + \cdots. \quad (11)$$

For flux zoning ($\Phi \propto s$), Eq. (11) can be used to obtain the linear extrapolation $X(0) = X(\Delta s) + [X(\Delta s) - X(2\Delta s)]$, whereas for $\Phi \propto s^2$, $X(0) = X(\Delta s)$ is adequate to obtain second-order accuracy in Δs. The asymptotic behavior of the components of R and Z for $m>2$ near the axis is imposed by requiring that $X(\Delta s) = X(2\Delta s)/2^{m/2}$ for $\Phi \propto s$ or $X(\Delta s) \simeq 0$ for $\Phi \propto s^2$.

To improve the temporal stability of the numerical scheme used to solve the MHD force equations, it is useful to accelerate the convergence of the magnetic axis, $X(0)$. To accomplish this acceleration, the $m=0$ components of R and Z (denoted $X_0(s, \zeta)$) are written

$$X_0(s, \zeta) = X_0(0, \zeta)(1 - \hat{\Phi}) + \tilde{X}_0(s, \zeta). \quad (12)$$

Here, $\tilde{X}_0(0, \zeta) = 0$ and $\hat{\Phi} = \Phi(s)/\Phi(1)$. Varying the magnetic energy with respect to $X_0(0, \zeta)$ yields the cross-section averaged force equation:

$$F(0) = \int (1 - \hat{\Phi}) F_0 \, ds, \tag{13}$$

where F_0 is the θ-averaged MHD force at the point (s, ζ). Since the highest order radial derivative term in F_0 can be written

$$F_0 \sim \frac{\partial}{\partial s} D_{xx} \frac{\partial}{\partial s} X_0(s, \zeta), \tag{14}$$

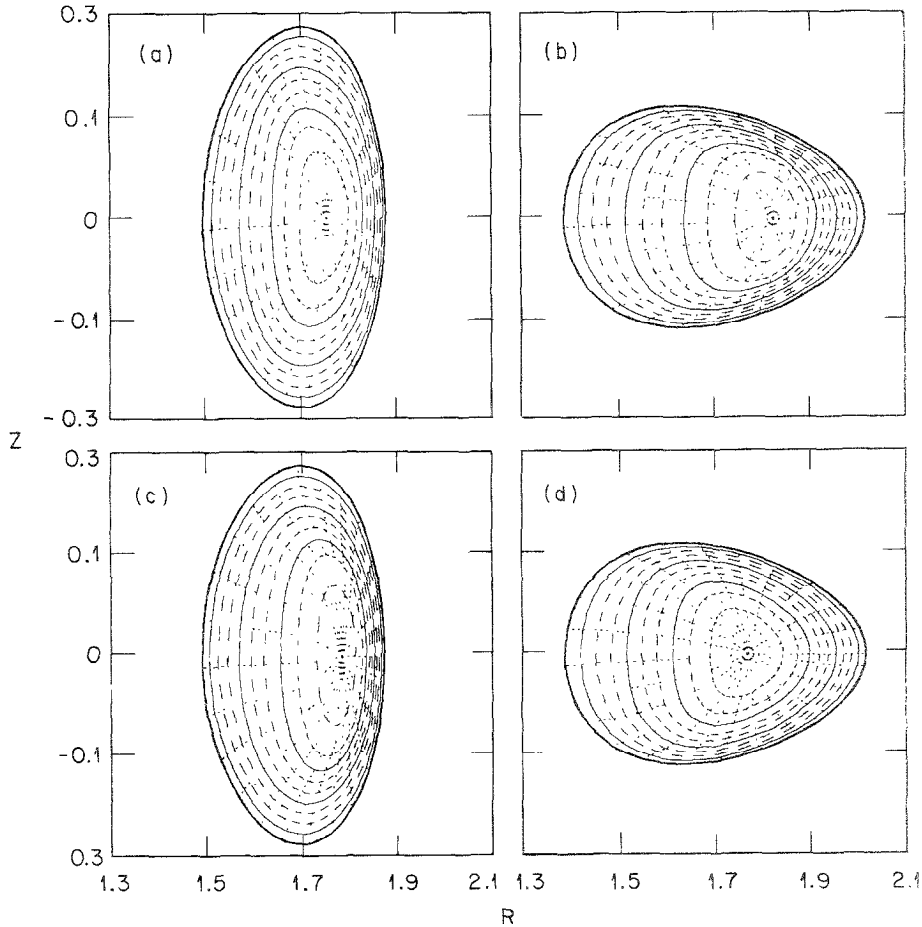

FIG. 1. Flux surfaces for the ATF device at $\langle \beta \rangle = 0.025$, on a mesh with $\Delta s = \frac{1}{8}$: (a) calculated by using scheme (I), toroidal angle $\phi = 0$; (b) scheme (I), $\phi = \pi/N_F$ ($N_F = 12$); (c) scheme (III), $\phi = 0$; (d) scheme (III), $\phi = \pi/N_F$.

Eq. (13) can be integrated by parts to yield

$$F(0) \simeq -\left(\int D_{xx}\, ds\right) X_0(0, \zeta). \tag{15}$$

Therefore, the eigenvalue in Eq. (15) is $\lambda_0 = -\int D_{xx}\, ds$, which is smaller by Δs^2 than the eigenvalues of the difference representation of Eq. (14). Thus, the temporal evolution of $X_0(0, \zeta)$ can be accelerated by $\Delta s^{-2} \gg 1$ without violating the Courant–Friedrichs–Lewy (CFL) numerical stability criterion.

4. Numerical Examples

The spatial convergence properties for the various schemes discussed in Section 2 are compared in this section. Since these properties are similar for schemes (II) and

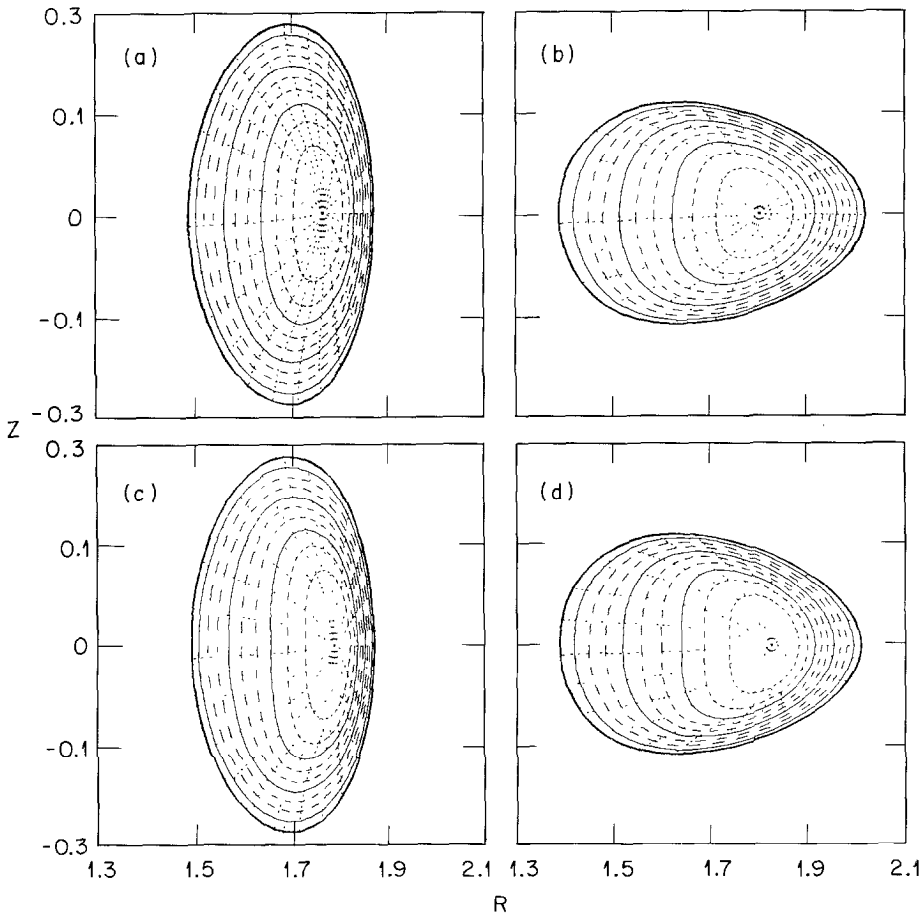

FIG. 2. Same as Fig. 1, with $\Delta s = \frac{1}{32}$.

(III), which both use half-mesh zoning for λ, we present only the results from the VMEC code [5] based on scheme (III) differencing. The equilibrium calculations described in this section have been performed by using the radial zoning appropriate to the respective differencing scheme. For scheme (I), Φ_2 zoning ($s \propto \sqrt{\Phi}$) yielded the best accuracy and most rapid temporal convergence. In contrast, Φ_1 zoning ($s \propto \Phi$) was preferable for schemes (II) and (III). In general, the computational time t_{cpu} increased with the number of radial mesh points N_s as $t_{\text{cpu}} \sim (N_s)^p$, where $p \lesssim 2$, but was nearly independent of the type of differencing scheme used.

Figures 1 and 2 compare the flux surfaces for a high-pressure ($\langle\beta\rangle \sim 0.025$) Advanced Toroidal Facility (ATF) equilibrium [11], calculated by using scheme (I) and scheme (III), for the two toroidal cross sections $\phi = 0$ and $\phi = \pi/N_F$. Here, $N_F = 12$ is the number of toroidal field periods for ATF. Figure 1 was computed by using the coarsest radial grid ($\Delta s = \frac{1}{8}$), and Fig. 2 shows the results for the finest mesh ($\Delta s = \frac{1}{32}$). It can be seen that the Shafranov shift and interior elongation are already quite accurately represented on the coarse grid for scheme (III) differencing. Both of these quantities undergo substantial changes from the coarse to the fine mesh for the scheme (I) case. Even on the finest mesh considered here, however, scheme (I) results are not yet well converged. This can be seen even more clearly in Figs. 3 and 4, which depict the convergence with radial mesh spacing of various equilibrium quantities. Figure 3 shows a convergence plot for the magnetic energy, W. Note that the $|\alpha_1|$ parameter, defined in Eq. (1), is just the slope of the curves in Fig. 3, and that $|\alpha_1^{\text{I}}| \gg |\alpha_1^{\text{III}}|$. In Fig. 4, the convergence for the mean magnetic axis, $R_{00}(0)$, and the peak pressure, $\beta(0)$, are shown. Once again, the relatively slower convergence of the scheme (I) results is apparent.

To demonstrate the effect of a strong helical axis on the spatial convergence

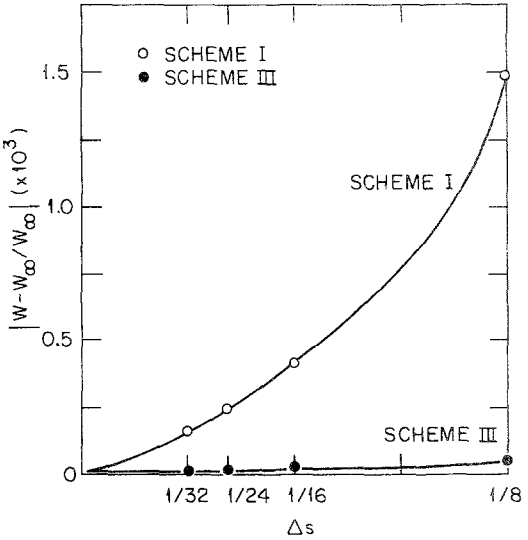

FIG. 3. Magnetic energy, W, vs square of the mesh spacing, Δs^2, for the ATF equilibrium in Fig. 1.

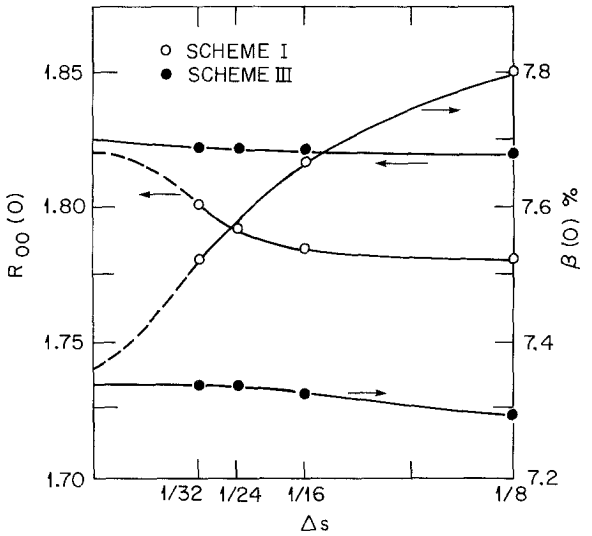

FIG. 4. Mean magnetic axis position, $R_{00}(0)$, and peak pressure, $\beta(0)$, vs square of the mesh spacing, Δs^2, for the ATF equilibrium in Fig. 1.

properties of the various differencing schemes, we considered the $N_F = 4$, $A = 10$ heliac configuration described in [12]. Convergence sequences for the rotational transform at the magnetic axis, $\iota(0)$, and the axis position $R_{00}(0)$ are shown in Fig. 5 for a plasma with $\langle\beta\rangle \simeq 0.02$. There is considerable variation with the mesh spacing Δs for the scheme (I) results, especially for $\iota(0)$. It is even difficult to predict an asymptotic value for $\iota(0)$ from the scheme (I) data for $\Delta s > \frac{1}{64}$.

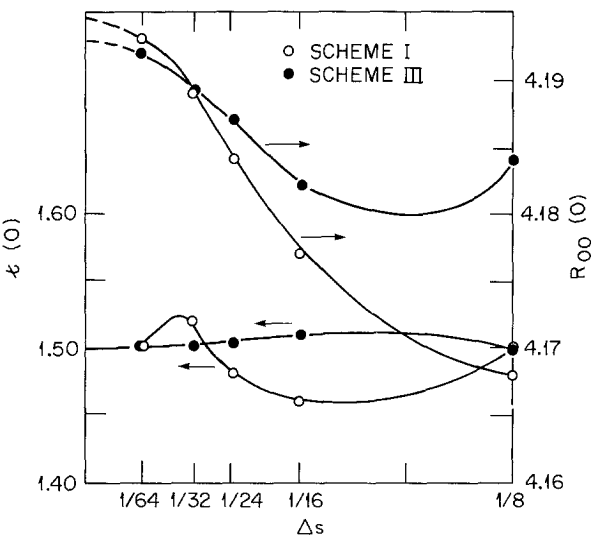

FIG. 5. Iota at plasma axis [$\iota(0)$] and plasma edge [$\iota(1)$] vs square of the mesh spacing, Δs^2, for the case of an equilibrium with strong helical axis.

5. Conclusions

Several schemes for discretizing the MHD forces have been compared. A new differencing scheme has been described that yields very accurate spatial resolution while remaining amenable to standard temporal descent solution methods.

References

1. S. P. Hirshman and D. K. Lee, *Comput. Phys. Commun.* **39**, 161 (1986).
2. U. Schwenn, *Comput. Phys. Commun.* **31**, 167 (1984); in *Proceedings, 5th International Workshop on Stellarators, Schloss Ringberg, 1984*, Comm. EC., EUR9618 EN, Vol. I, p. 377.
3. L. Lao, *Comput. Phys. Commun.* **31**, 201 (1984).
4. A. Bhattacharjee, J. C. Wiley, and R. L. Dewar, *Comput. Phys. Commun.* **31**, 201 (1984).
5. S. P. Hirshman, W. I. Van Rij, and P. Merkel, *Comput. Phys. Commun.* **43**, 143 (1986).
6. O. Betancourt, *Comments Pure Appl. Math.* **41**, 551 (1988).
7. S. P. Hirshman and J. T. Hogan, *J. Comput. Phys.* **63**, 329 (1986).
8. J. Nührenberg, R. Zille, and S. P. Hirshman, "Resistively Stable Stellarator Equilibria by β Iteration," in *8th Europhysics Conference on Computational Physics Computing in Plasma Physics, Federal Rep. of Germany, May, 1986*, p. 48.
9. L. L. Lao, S. P. Hirshman, and R. M. Wieland, *Phys. Fluids* **24**, 1431 (1981).
10. K. Ling and S. C. Jardin, *J. Comput. Phys.* **58**, 300 (1985).
11. J. F. Lyon *et al.*, *Fusion Technol.* **10**, 179 (1986).
12. A. H. Boozer, *Phys. Fluids* **24**, 1999 (1981).